

Structural and magnetic properties of β -Li₂IrO₃ after grazing-angle focused ion beam thinning

Nelson Hua, Franziska Breitner, Anton Jesche, Shih-Wen Huang, Christian Rüegg, Philipp Gegenwart

Angaben zur Veröffentlichung / Publication details:

Hua, Nelson, Franziska Breitner, Anton Jesche, Shih-Wen Huang, Christian Rüegg, and Philipp Gegenwart. 2025. "Structural and magnetic properties of β -Li₂IrO₃ after grazing-angle focused ion beam thinning." Acta Crystallographica: Section B, Structural science, crystal engineering and materials 81 (2): 202-7.
<https://doi.org/10.1107/S2052520625000587>.



Structural and magnetic properties of β -Li₂IrO₃ after grazing-angle focused ion beam thinning

Nelson Hua,^{a,b,*} Franziska Breitner,^c Anton Jesche,^c Shih-Wen Huang,^a Christian Rüegg^{a,b,d,e} and Philipp Gegenwart^{c,*}

^aPSI Center for Photon Science, Paul Scherrer Institute, 5232 Villigen PSI, Switzerland, ^bInstitute for Quantum Electronics, ETH Zürich, CH-8093 Hônggerberg, Switzerland, ^cExperimental Physics VI, Center for Electronic Correlations and Magnetism, University of Augsburg, 86135 Augsburg, Germany, ^dInstitute of Physics, Ecole Polytechnique Fédérale de Lausanne (EPFL), CH-1015 Lausanne, Switzerland, and ^eDepartment of Quantum Matter Physics, University of Geneva, CH-1211 Geneva, Switzerland. *Correspondence e-mail: nelson.hua@psi.ch, philipp.gegenwart@physik.uni-augsburg.de

Received 20 January 2025

Accepted 21 January 2025

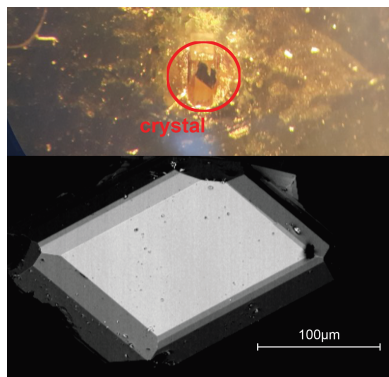
Edited by M. Dusek, Academy of Sciences of the Czech Republic, Czechia

Keywords: focused-ion beam; magnetic diffraction; sample fabrication; X-ray diffraction.

Manipulating the size and orientation of quantum materials is often used to tune emergent phenomena, but precise control of these parameters is also necessary from an experimental point of view. Various synthesis techniques already exist, such as epitaxial thin film growth and chemical etching, that are capable of producing specific sample dimensions with high precision. However, certain materials exist as single crystals that are often difficult to manipulate, thereby limiting their studies to a certain subset of experimental techniques. One particular class of these materials includes lithium and sodium iridates, which are promising candidates for hosting a Kitaev quantum spin liquid state. Here a controlled method of using a focused ion beam at grazing incidence to reduce the size of a β -Li₂IrO₃ single crystal to a thickness of 1–2 μ m is presented. Subsequent X-ray diffraction measurements show the lattice remains intact, albeit with a larger mosaic spread. The integrity of the magnetic order is also preserved as the temperature dependent magnetic diffraction peak follows the same trend as its bulk counterpart with a transition temperature at $T_N = 37.5$ K. Our study demonstrates a technique that opens up the possibility of nonequilibrium experiments where submicron thin samples are often essential.

1. Introduction

Enhancing certain order parameters and material properties by reducing dimensionality is a common avenue in engineering quantum materials (Giustino *et al.*, 2021; Ahn *et al.*, 2021; Lei *et al.*, 2017). For example, one can drastically increase the superconducting temperature of FeSe from $T_c = 8$ K to 65 K by going from a bulk crystal to a single monolayer grown on SrTiO₃ (Wang *et al.*, 2012; He *et al.*, 2013; Kitamura *et al.*, 2022). In one dimension, a possible path to the realization of the topological Kondo effect has been proposed by intertwining nanowires nearby a superconducting island (Béri & Cooper, 2012; Altland & Egger, 2013). Even extending to zero-dimensional objects can give rise to peculiar properties. Confinement effects that lead to enhanced optoelectronic properties in semiconducting materials can be achieved as quantum dots where the material is reduced to a few nanometres in all directions (Veldhorst *et al.*, 2015; de Arquer *et al.*, 2021). These materials can be further modified with intentional or consequential defects such as strain or impurities. Nanoislands of La_{0.7}Sr_{0.3}MnO₃ have been synthesized from electron beam lithography with the aid of Ar⁺ ion implantation that modifies the strain state, consequently enhancing the flux closure domains (Takamura *et al.*, 2006). Introducing



Published under a CC BY 4.0 licence

defects such as screw dislocations can also improve the performance of lithium-rich battery nanoparticles (Ulvestad *et al.*, 2015; Singer *et al.*, 2018). The numerous existing synthesis routes have even opened up the possibility of using artificial intelligence to find optimized methods for tuning material properties (Stanev *et al.*, 2021; Yan *et al.*, 2023).

On the other hand, understanding intrinsic material properties from a fundamental physics point of view often requires stringent conditions to accurately deduce the origins of emergent phenomena where the flexibility of engineering is no longer suitable. This requires the use of several complementary experimental techniques that would ideally use the same sample for all measurements, which is rarely the case. For example, we want to ensure the thin lamella sample used for transmission electron microscopy retains the same properties as the bulk crystal used for neutron scattering. This is difficult to carry out if unwanted dopants or defects are introduced in creating the lamella from the bulk sample. This also implies that thin films and bulk crystals can not always be accurately compared due to substrate-induced strain (Liu *et al.*, 2014; Liu *et al.*, 2016), and samples that have been processed with chemical etching may show different lattice constants due to implantation of another chemical species (Takamura *et al.*, 2006). Furthermore, limitations such as a large lattice mismatch between the sample and substrate preclude the option of epitaxial film growth for many materials. Even when the same sample is used across different measurements, certain surface sensitive techniques may not capture the properties that are characteristic of the bulk. This is particularly noted in topological insulators where the metallic surface states do not reflect the internal insulating properties (Moore, 2010). Therefore, consideration of sample integrity across complementary experimental techniques is essential in studying inherent material properties. Here we present a minimally invasive use of a focused ion beam (FIB) to reduce the size of a β - Li_2IrO_3 crystal. The FIB-processed crystal is reduced to a minimum thickness of 1 μm and maintains its structural and magnetic properties, opening more investigative routes with experimental techniques that were previously inaccessible.

β - Li_2IrO_3 belongs to the class of Kitaev materials, meaning it displays bond-dependent anisotropic spin exchange, though additional exchanges lead to deviations from pure Kitaev physics (Takayama *et al.*, 2015; Biffin *et al.*, 2014; Ruiz *et al.*, 2017; Freund *et al.*, 2016; Tsirlin & Gegenwart, 2022). The β -polymorph with a hyperhoneycomb lattice of Ir moments exhibits an incommensurate magnetic order below $T_N = 37$ – 38 K (Takayama *et al.*, 2015; Tsirlin & Gegenwart, 2022). Compared to other prominent Kitaev materials such as α - RuCl_3 (Sears *et al.*, 2020) or honeycomb iridates $A_2\text{IrO}_3$ ($A = \text{Na}, \text{Li}$) (Tsirlin & Gegenwart, 2022) that order below 15 K, the elevated Néel temperature allows easier access to the ground state by dissipative pump-probe experiments. Since its relatively recent synthesis, β - Li_2IrO_3 has been studied with X-rays, neutrons, and muons under high-pressures and high magnetic fields (Takayama *et al.*, 2015; Biffin *et al.*, 2014; Ruiz *et al.*, 2017; Majumder *et al.*, 2018; Majumder *et al.*, 2019), but only a few time-resolved experiments have

looked into the dynamics and excitations in this material (Glamazda *et al.*, 2016; Choi *et al.*, 2020). Techniques such as ultrafast electron diffraction or time-resolved X-ray scattering can reveal dynamics of the structural and magnetic order parameters that can indirectly reveal bond-dependent interaction strengths of the correlated state (Rademaker, 2019; Bragança *et al.*, 2021). However, a significant limitation is the thickness of single crystals that is often incompatible with time-resolved scattering techniques that rely on submicron thin samples. Opening these time-resolved experimental paths requires reducing these crystal thicknesses in a controlled manner.

2. Sample and technique

For layered materials, thin flakes can often be easily prepared by exfoliation until the desired thickness is reached. However, this does not work for β - Li_2IrO_3 as the material does not cleave easily due to its three-dimensional structure. Another common possibility is to use a FIB for cutting a thin lamella (Moll, 2018). We attempted this standard milling process for β - Li_2IrO_3 with the FIB-SEM Crossbeam 500 (Zeiss), but this approach proved infeasible due to internal cracks uncovered during cutting or lamella breakage during thinning or transfer. Therefore, a different approach was required where we used the FIB-SEM to thin down the crystals by small-angle Ga-beam bombardment. A suitable crystal of sufficiently large size with distinct surfaces to assign the crystal axes by eye was chosen. After one of the surfaces perpendicular to the c axis was polished, the crystal was glued onto an SrTiO_3 (STO) substrate (5×10 mm) with the polished surface facing down using two-component epoxy (Araldite Rapid) and cured at 100°C for 1 h. The crystal was mounted 1 mm away from any edge to accommodate alignment requirements for future

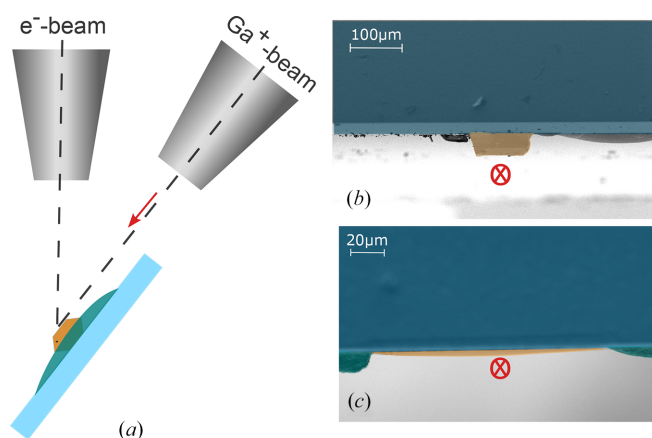


Figure 1
(a) The β - Li_2IrO_3 crystal (orange) was glued onto an STO substrate (light blue) using epoxy glue (teal), mounted on a pre-tilted sample holder and aligned with the surface parallel to the Ga^+ ion beam. An e^- beam was subsequently used to remove Ga implantations. Side view of the (b) unprocessed sample and (c) thinned sample along the ion beam (indicated by the direction of the red arrow in (a), which is also shown in red in (b) and (c) perpendicular to the picture plane).

experiments. Before mounting the sample onto a pre-tilted sample holder, the sample was polished down further in order to reduce the required time of Ga beam operation. We subsequently oriented the sample in the sample chamber such that the ion beam cut parallel to the sample surface, as can be seen in Fig. 1(a).

Using first a voltage of 30 kV and high probe currents up to 65 nA, the sample was thinned, as shown in Figs. 1(b) and 1(c). In the latter stages, progressively smaller currents were applied before finally removing possible Ga implantations by performing low-energy milling. In this way, an area of approximately $50\ \mu\text{m} \times 50\ \mu\text{m}$ was thinned down to an average thickness of about $2\ \mu\text{m}$, with some areas down to $1\ \mu\text{m}$. Attempts to further thin the sample resulted in the onset of peeling at the edges of the crystal. Thus, no further thinning of the sample depicted in Figs. 2(a)–2(c) was performed. For comparison, an untreated, bulk crystal with a surface area of about $100\ \mu\text{m} \times 150\ \mu\text{m}$ and a thickness of $50\ \mu\text{m}$, as depicted

in Fig. 2(d), was mounted onto an STO substrate with the *c*-axis orientated perpendicular to the substrate surface.

3. Experiment and results

The X-ray diffraction experiment on the bulk and FIB-processed $\beta\text{-Li}_2\text{IrO}_3$ crystals was carried out at the Materials Science Surface Diffraction (X04SA) beamline of the Swiss Light Source (Willmott *et al.*, 2013). The X-ray energy was tuned to 11.115 keV to measure the (004) and (135) lattice peaks at room temperature while 11.215 keV was used to measure the incommensurate $(-0.584, 0, 16)$ magnetic peak at the Ir L_3 -edge resonance. We followed the evolution of the magnetic peak in the FIB-processed crystal between 15.0 and 37.5 K, which can only be detected at resonance below T_N . Both crystals were aligned with the *c* axis out of plane and the diffraction signals were recorded on a 0.5M Eiger detector with $75\ \mu\text{m}$ pixel sizes. The experimental geometry follows a standard (2+3) surface diffractometer where the 2D detector is fixed approximately 1 m from the sample and moves along a spherical surface in the 2θ and δ directions.

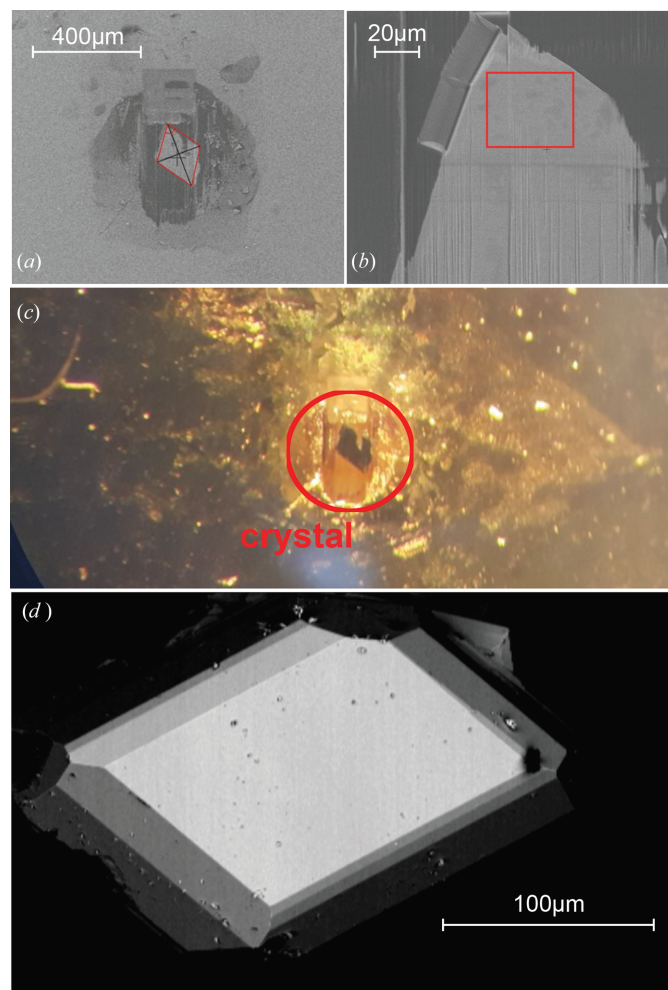


Figure 2
(a, b) The FIB processed sample of $\beta\text{-Li}_2\text{IrO}_3$ under an optical microscope for two different magnifications. The red rectangle in (b) marks the measurement area while (c) shows the FIB processed sample on a gold covered STO substrate used for the X-ray diffraction measurements. (d) A separate $\beta\text{-Li}_2\text{IrO}_3$ bulk crystal was also prepared as a reference, and characterized with X-ray diffraction.

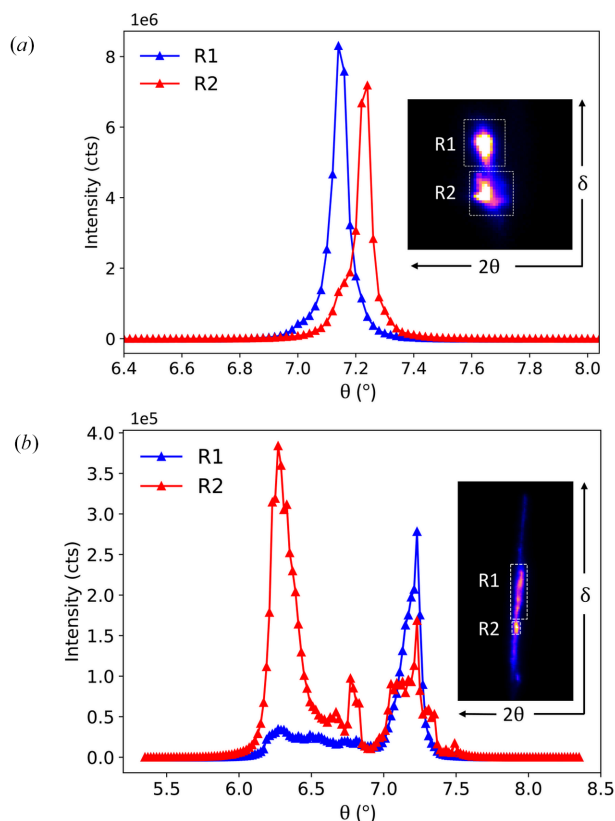


Figure 3
(a) Rocking curve of the bulk crystal (004) lattice peak that is split into two domains designated as R1 and R2. (Inset) The two peaks appear at the same 2θ value of the detector, but at a different δ value. (b) The (004) lattice peak of the FIB-processed crystal shows multiple domains and the corresponding summed detector image is shown in the inset. Two principal regions are designated as R1 and R2. The structural effects due to the FIB processing can be seen in the elongated diffuse scattering on the detector.

The (004) diffraction peak directly probes the out-of-plane lattice structure, including the crystallographic c -axis lattice constant. The measured lattice constants from the (004) peak of the bulk and the FIB-processed samples were 1.783 Å and 1.787 Å, respectively. These are in line with previously reported values of 1.779 Å (Biffin *et al.*, 2014) and 1.786 Å (Ruiz *et al.*, 2017). As seen in Fig. 3(a), the (004) lattice peak is split on the detector along the δ direction and with a slight offset in the incidence angle θ . This shows that our bulk crystal consists of two principal domains that are slightly tilted from each other. However, their 2θ values are the same, indicating both domains have the same lattice constant. Fig. 3(b) shows the (004) lattice peak profile of the FIB-processed sample that is broken into several domains. The rocking curves of two regions of interest on the detector, designated as R1 and R2 in the inset, are shown where the diffraction peak is spread along approximately the same 2θ value. Therefore, these domains share the same lattice constant, but the larger spread in the sample θ and detector δ directions directly translates to a larger mosaic spread, as can be seen in the diffuse tails. In other words, the FIB process introduced many smaller domains that are slightly tilted, and therefore form a partial ‘powder’ diffraction ring.

The (135) lattice peak probes both the in-plane and out-of-plane lattice integrity where the rocking curves for the bulk and FIB-processed crystals are shown in Fig. 4(a) and 4(b), respectively. Similar to the (004) lattice peak, the (135) lattice peak of the bulk crystal shows up at two sample θ angles and two locations on the detector, indicating two principal domains. On the other hand, the FIB-processed crystal shows primarily one wide, continuous peak in both the sample θ angle and on the detector, indicative of a mosaic spread with small domain sizes.

To compare the effects of our technique quantitatively, both the (004) and (135) lattice peaks of the bulk and FIB-processed crystals were fitted with single and double pseudo-Voigt functions. Fig. 5(a) shows the (004) lattice peak of the bulk crystal R2 domain superimposed on the FIB-processed crystal R1 domain, along with their fits from a double pseudo-Voigt function to take into account the shoulders at the smaller θ angles. The full width half maximums (FWHMs) of the sharper peaks at the higher θ values from the fits are 0.0414° for the FIB-processed crystal and 0.0425° for the bulk crystal. Since our experimental resolution is 0.02° , the out-of-

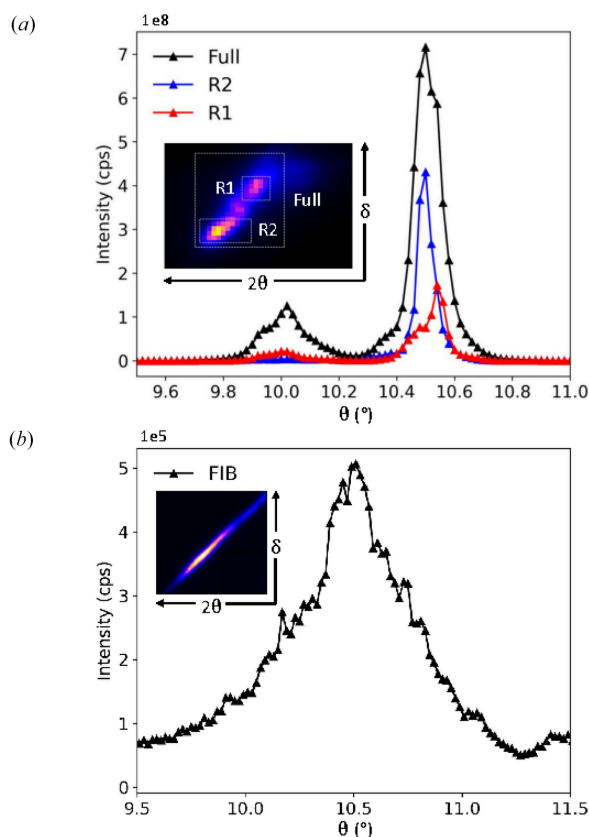


Figure 4
(a) Rocking curve of the bulk crystal (135) lattice peak and the corresponding detector regions of interest, R1 and R2, shown in the inset. As with the (004) lattice peak, this indicates two primary structural domains in the single crystal. (b) The (135) lattice peak of the FIB-processed crystal exhibits a large mosaic spread, suggesting many smaller domains that are slightly tilted. This results in the partial powder diffraction ring that forms.

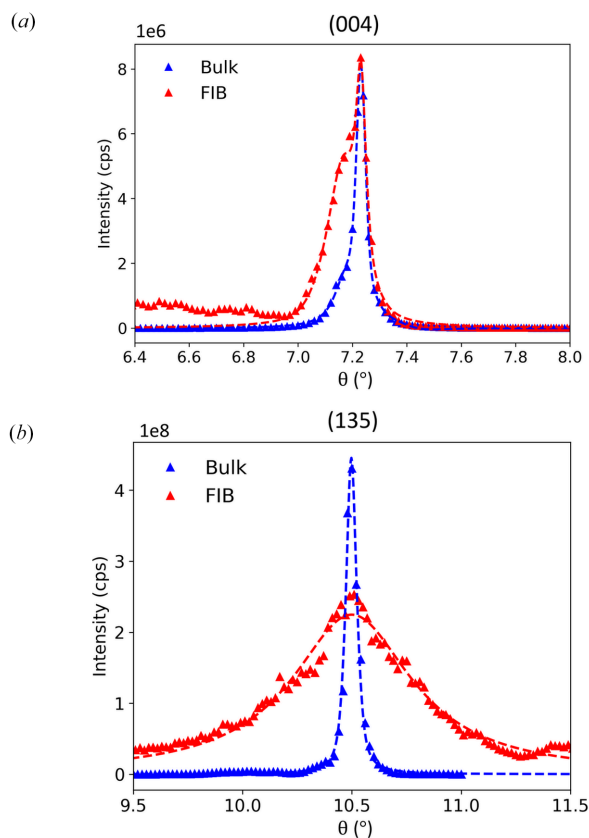


Figure 5
(a) The (004) lattice peak of the bulk crystal R2 domain superimposed on the corresponding R1 domain of the FIB-processed crystal (magnified by $30\times$). A double pseudo-Voigt function was used as a fit to take into account the shoulder. (b) The (135) lattice peak of the bulk crystal R1 domain superimposed on the corresponding FIB-processed crystal lattice peak (magnified by $500\times$). Both peaks were fitted with a single pseudo-Voigt function. The correlation length of the bulk crystal (135) lattice peak is approximately an order of magnitude larger than the FIB-processed crystal.

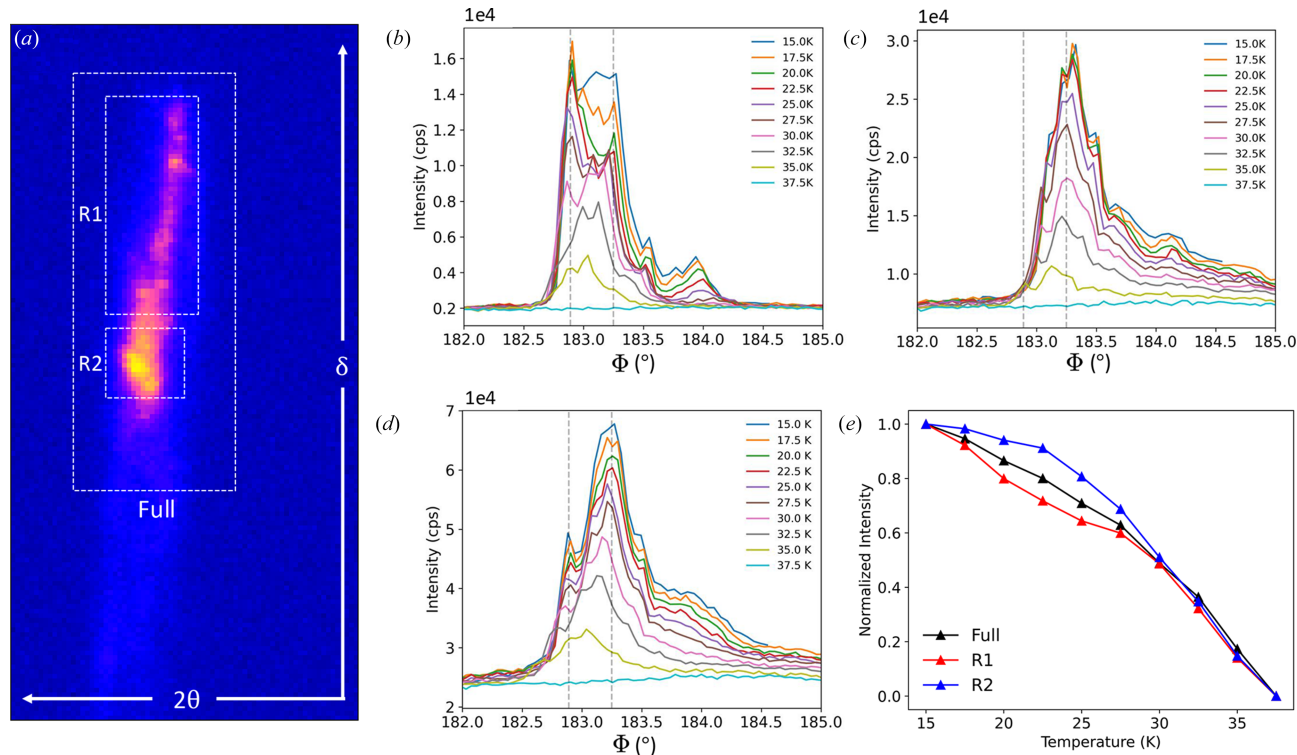


Figure 6 (a) The summed detector image of a rocking curve on the $(-0.584, 0, 16)$ magnetic peak at $T = 15$ K. The rocking curves of the (b) R1, (c) R2, and the (d) full diffraction peak regions of interest between 15.0 and 37.5 K are shown. The vertical dotted lines are reference lines to compare notable peaks for the two regions of interest, corresponding to larger domains of the FIB-processed crystal. (e) The normalized integrated intensity of the regions of interest as a function of temperature are shown for the detector regions of interest. The disappearance of the magnetic diffraction peak at $T = 37.5$ K for the FIB-processed crystal is in agreement with previous studies for bulk crystals.

plane correlation lengths are effectively the same. Fig. 5(b) shows the (135) lattice peaks of the bulk crystal R1 domain and the FIB-processed crystal along with their single pseudo-Voigt fits. The FWHM of the bulk crystal diffraction peak is 0.068° whereas the FWHM of the FIB-processed crystal diffraction peak is 0.600° , which is a 9.4 times larger correlation length for the bulk crystal. The much larger change in correlation length of the (135) lattice peak suggests that our FIB technique induces a significant change to the in-plane structural integrity compared of the out-of-plane lattice structure.

Finally, the magnetic structure of the FIB-processed crystal was studied via the incommensurate $(-0.584, 0, 16)$ resonant magnetic peak. The summed detector image of a rocking curve at $T = 15$ K is shown in Fig. 6(a). Here the diffraction peak is again broadened along the same 2θ value, which is in line with the (004) lattice structure as the diffraction geometry of the magnetic structure is almost specular. This suggests that the boundaries of the magnetic domain structure are defined by the structural domains. The rocking curves of the incommensurate peak was performed by rotating Φ , the azimuthal angle about the c -axis lattice direction, to maintain a constant penetration depth. The rocking curves for the regions of interest, defined as R1, R2 and the full diffraction peak in Fig. 6(a), are shown in Figs. 6(b)–6(d) for the temperature range between 15.0 and 37.5 K. The normalized integrated

intensity from these rocking curves are shown in Fig. 6(e) where the peak disappears completely at $T = 37.5$ K. This aligns well with previously measured transition temperatures for a single crystal at $T_N = 37\text{--}38$ K (Tsirlin & Gegenwart, 2022; Ruiz *et al.*, 2017).

4. Conclusion

We have demonstrated a controlled, FIB-based technique that is capable of reducing the thickness of $\beta\text{-Li}_2\text{IrO}_3$ crystals. Since this material neither easily cleaves nor allows FIB-assisted thin lamella cutting, the new technique provides a unique possibility to obtain $\beta\text{-Li}_2\text{IrO}_3$ crystal thicknesses down to ~ 1 μm . As expected, the processed crystal exhibits a larger mosaic spread due to smaller domains not present in the original bulk crystal. This is attributed to the effects of the Ga^+ ion beam from the FIB process. The subsequent e-beam milling used to remove possible Ga implantation and dopants likely also contributes to the degraded structural integrity. The c -axis lattice constant of the FIB-processed crystal is also in line with previously measured values from bulk samples, suggesting that the FIB process did not introduce enough dopants that would have significantly strained the sample. However, proper fluorescence measurements are needed to quantify the final composition.

While the structural quality of the FIB-processed β -Li₂IrO₃ crystal is partially compromised compared to that of the bulk crystal, as seen from broadened lattice diffraction peaks and diffuse scattering tails, the electronic structure of the material, namely the magnetically ordered state, is still preserved. The magnetic transition temperature of the FIB-processed β -Li₂IrO₃ crystal is in line with previous results on bulk crystals, and the similarity of the elongated diffuse tails between the (−0.584, 0, 16) magnetic and (004) lattice peaks suggest that while the FIB process created smaller structural domains, the magnetic order within those domains are retained. Currently the most significant limitation of this technique is the onset of peeling as the sample approaches nanometre thicknesses, but further improvements to this technique in the future can result in crystal sizes with a thickness of several hundred nanometres. Extending this to other materials where neither cleaving nor thin lamella preparation is possible will open the possibility of time-resolved experiments such as ultrafast electron diffraction or pump-probe X-ray diffraction measurements.

Acknowledgements

We acknowledge the Paul Scherrer Institut, Villigen, Switzerland for provision of synchrotron radiation beamtime at beamline X04SA of the SLS. Open access funding enabled and organized by Projekt DEAL.

Funding information

The following funding is acknowledged: H2020 Marie Skłodowska-Curie Actions [grant No. 884104 to Nelson Hua (PSI-FELLOW-III-3i)]; Deutsche Forschungsgemeinschaft (grant No. TRR 360 – 492547816 to Franziska Breitner, Philipp Gegenwart, Anton Jesche).

References

Ahn, C., Cavalleri, A., Georges, A., Ismail-Beigi, S., Millis, A. J. & Triscone, J.-M. (2021). *Nat. Mater.* **20**, 1462–1468.

Altland, A. & Egger, R. (2013). *Phys. Rev. Lett.* **110**, 196401.

Arquer, F. P. G. de, Talapin, D. V., Klimov, V. I., Arakawa, Y., Bayer, M. & Sargent, E. H. (2021). *Science*, **373**, eaaz8541.

Béri, B. & Cooper, N. R. (2012). *Phys. Rev. Lett.* **109**, 156803.

Biffin, A., Johnson, R. D., Choi, S., Freund, F., Manni, S., Bombardi, A., Manuel, P., Gegenwart, P. & Coldea, R. (2014). *Phys. Rev. B*, **90**, 205116.

Bragança, H., Cavalcante, M. F., Pereira, R. G. & Aguiar, M. C. O. (2021). *Phys. Rev. B*, **103**, 125152.

Choi, S., Kim, H.-S., Kim, H.-H., Krajewska, A., Kim, G., Minola, M., Takayama, T., Takagi, H., Haule, K., Vanderbilt, D. & Keimer, B. (2020). *Phys. Rev. B*, **101**, 054102.

Freund, F., Williams, S. C., Johnson, R. D., Coldea, R., Gegenwart, P. & Jesche, A. (2016). *Sci. Rep.* **6**, 35362.

Giustino, F., Lee, J. H., Trier, F., Bibes, M., Winter, S. M., Valentí, R., Son, Y.-W., Taillifer, L., Heil, C., McIver, A. I., Torres, L. E. F. F., Low, T., Kumar, A., Galceran, R., Valenzuela, S. O., Costache, M.

V., Manchon, A., Kim, E.-A., Schleder, G. R., Fazzio, A. & Roche, S. (2021). *J. Phys. Mater.* **3**, 042006.

Glamazda, A., Lemmens, P., Do, S. H., Choi, Y. S. & Choi, K. Y. (2016). *Nat. Commun.* **7**, 12286.

He, S., He, J., Zhang, W., Zhao, L., Liu, D., Liu, X., Mou, D., Ou, Y.-B., Wang, Q.-Y., Li, Z., Wang, L., Peng, Y., Liu, Y., Chen, C., Yu, L., Liu, G., Dong, X., Zhang, J., Chen, C., Xu, Z., Chen, X., Ma, X., Xue, Q. & Zhou, X. J. (2013). *Nat. Mater.* **12**, 605–610.

Kitamura, T., Yamashita, T., Ishizuka, J., Daido, A. & Yanase, Y. (2022). *Phys. Rev. Res.* **4**, 023232.

Lei, Q., Golalikhani, M., Davidson, B. A., Liu, G., Schlom, D. G., Qiao, Q., Zhu, Y., Chandrasena, R. U., Yang, W., Gray, A. X., Arenholz, E., Farrar, A. K., Tenne, D. A., Hu, M., Guo, J., Singh, R. K. & Xi, X. (2017). *npj Quant. Mater.* **2**, 10.

Liu, X., Chang, C.-F., Rata, A. D., Komarek, A. C. & Tjeng, L. H. (2016). *npj Quantum Materials* **1**, 16027.

Liu, X. H., Rata, A. D., Chang, C. F., Komarek, A. C. & Tjeng, L. H. (2014). *Phys. Rev. B*, **90**, 125142.

Majumder, M., Freund, F., Dey, T., Prinz-Zwick, M., Büttgen, N., Skourski, Y., Jesche, A., Tsirlin, A. A. & Gegenwart, P. (2019). *Phys. Rev. Mater.* **3**, 074408.

Majumder, M., Manna, R. S., Simutis, G., Orain, J. C., Dey, T., Freund, F., Jesche, A., Khasanov, R., Biswas, P. K., Bykova, E., Dubrovinskaia, N., Dubrovinsky, L. S., Yadav, R., Hozoi, L., Nishimoto, S., Tsirlin, A. A. & Gegenwart, P. (2018). *Phys. Rev. Lett.* **120**, 237202.

Moll, P. J. (2018). *Annu. Rev. Condens. Matter Phys.* **9**, 147–162.

Moore, J. E. (2010). *Nature*, **464**, 194–198.

Rademaker, L. (2019). *SciPost Phys.* **7**, 071.

Ruiz, A., Frano, A., Breznay, N. P., Kimchi, I., Helm, T., Oswald, I., Chan, J. Y., Birgeneau, R. J., Islam, Z. & Analytis, J. G. (2017). *Nat. Commun.* **8**, 961.

Sears, J. A., Chern, L. E., Kim, S., Bereciartua, P. J., Francoual, S., Kim, Y. B. & Kim, Y.-J. (2020). *Nat. Phys.* **16**, 837–840.

Singer, A., Zhang, M., Hy, S., Cela, D., Fang, C., Wynn, T. A., Qiu, B., Xia, Y., Liu, Z., Ulvestad, A., Hua, N., Wingert, J., Liu, H., Sprung, M., Zozulya, A. V., Maxey, E., Harder, R., Meng, Y. S. & Shpyrko, O. G. (2018). *Nat. Energ.* **3**, 641–647.

Stanev, V., Choudhary, K., Kusne, A. G., Paglione, J. & Takeuchi, I. (2021). *Commun. Mater.* **2**, 105.

Takamura, Y., Chopdekar, R. V., Scholl, A., Doran, A., Liddle, J. A., Harteneck, B. & Suzuki, Y. (2006). *Nano Lett.* **6**, 1287–1291.

Takayama, T., Kato, A., Dinnebier, R., Nuss, J., Kono, H., Veiga, L. S. I., Fabbri, G., Haskel, D. & Takagi, H. (2015). *Phys. Rev. Lett.* **114**, 077202.

Tsirlin, A. A. & Gegenwart, P. (2022). *Phys. Status Solidi B*, **259**, 2100146.

Ulvestad, A., Singer, A., Clark, J. N., Cho, H. M., Kim, J. W., Harder, R., Maser, J., Meng, Y. S. & Shpyrko, O. G. (2015). *Science*, **348**, 1344–1347.

Veldhorst, M., Yang, C. H., Hwang, J. C. C., Huang, W., Dehollain, J. P., Muhonen, J. T., Simmons, S., Laucht, A., Hudson, F. E., Itoh, K. M., Morello, A. & Dzurak, A. S. (2015). *Nature*, **526**, 410–414.

Wang, Q.-Y., Li, Z., Zhang, W.-H., Zhang, Z.-C., Zhang, J.-S., Li, W., Ding, H., Ou, Y.-B., Deng, P., Chang, K., Wen, J., Song, C., He, K., Jia, J., Ji, S., Wang, Y., Wang, L., Chen, X., Ma, X. & Xue, Q. (2012). *Chin. Phys. Lett.* **29**, 037402.

Willmott, P. R., Meister, D., Leake, S. J., Lange, M., Bergamaschi, A., Böge, M., Calvi, M., Cancellieri, C., Casati, N., Cervellino, A., Chen, Q., David, C., Flechsig, U., Gozzo, F., Henrich, B., Jäggi-Spielmann, S., Jakob, B., Kalichava, I., Karvinen, P., Krempasky, J., Lüdeke, A., Lüscher, R., Maag, S., Quitmann, C., Reinle-Schmitt, M. L., Schmidt, T., Schmitt, B., Streun, A., Vartiainen, I., Vitins, M., Wang, X. & Wulfschleger, R. (2013). *J. Synchrotron Rad.* **20**, 667–682.

Yan, D., Smith, A. D. & Chen, C.-C. (2023). *Nat. Comput. Sci.* **3**, 572–574.